Applied Physics Letters

Understanding how non-condensable gases modify cavitation mass transfer through the van der Waals theory of capillarity

Cite as: Appl. Phys. Lett. **117**, 204102 (2020); https://doi.org/10.1063/5.0021697
Submitted: 13 July 2020 . Accepted: 11 November 2020 . Published Online: 19 November 2020

Saikat Mukherjee, and Hector Gomez

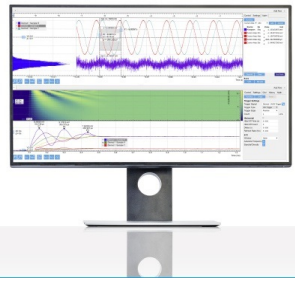

AIP Publishing

Applied Physics Letters ARTICLE scitation.org/journal/apl

Understanding how non-condensable gases modify cavitation mass transfer through the van der Waals theory of capillarity

Cite as: Appl. Phys. Lett. **117**, 204102 (2020); doi: 10.1063/5.0021697
Submitted: 13 July 2020 · Accepted: 11 November 2020 ·
Published Online: 19 November 2020

Saikat Mukherjee[a] and Hector Gomez

AFFILIATIONS

School of Mechanical Engineering, Purdue University, 585 Purdue Mall, West Lafayette, Indiana 47907, USA

[a]Author to whom correspondence should be addressed: mukher32@purdue.edu

ABSTRACT

Cavitation of a pure fluid continues to be a challenging problem in fluid dynamics. However, most cavitating fluids contain small amounts of non-condensable gases that can change the dynamics of the process significantly. While the effect of non-condensable gases on the surface and bulk properties of the fluid has been studied in detail, its impact on liquid–vapor mass transfer has remained elusive. Here, we provide mechanistic insight into this process using theory and simulations. Our results point to a dual role of non-condensable gases on liquid–vapor mass transfer. While the presence of non-condensable gases always reduces hydrodynamic cavitation, it also leads to a mass transfer mechanism that we call mixing cavitation. We show that mixing cavitation may increase or reduce mass transfer under different physical conditions and can dominate hydrodynamic cavitation. This study opens possibilities to better understand cavitation inception.

Cavitation is a liquid–vapor phase transformation driven by depressurization. Understanding cavitation is of great interest not only in physics but also in engineering,[1] biology,[2,3] and medicine.[4] Although the study of cavitation of a pristine fluid is essential, the cavitating fluid usually contains non-condensable gases (NCG). The NCG can be present in dissolution or in the form of nanometer-sized nuclei that are believed to remain stable for long times.[5,6] While the presence of NCG in water has been used to reconcile theoretical[7] and experimental[8] estimates of the tensile strength of water, the mechanisms whereby NCG modify the rate of liquid–vapor mass transfer when the phase-transforming fluid cavitates remain poorly understood. This knowledge gap can be partially attributed to our limited ability to experimentally measure the concentration of NCG in the phase-transforming fluid.[9] Precise measurements of NCG concentration are difficult in the liquid phase of the phase-transforming fluid, but even more challenging in its vapor phase.

Here, we show through theory and simulations that NCG modify liquid–vapor mass transfer by two mechanisms: The first one always results in a lower rate of mass transfer from liquid to vapor and is explained by an NCG-induced reduction of hydrodynamic cavitation. The second one, however, may increase or reduce mass transfer and depends primarily on the mixing dynamics of the NCG with the phase-transforming fluid. We call this mechanism mixing cavitation. We find that mixing cavitation can be the primary contributor to mass transfer in the presence of gas nuclei.

Our model is based on the phase-field theory. This approach allows us to model cavitation without any pre-defined phase-change criterion and quantitatively agrees with benchmarks and experiments in single-component liquid–vapor phase transformations.[10] The phase-field method, thus, provides a unique opportunity to fundamentally understand the role of NCG on cavitation. We derive our model from a free-energy functional. For isothermal conditions, the free-energy density of a fluid mixture with density ρ, and NCG concentration c, takes on the form

$$\Psi_M(\rho, c) = \Psi_V(\rho) + \frac{1}{M_s} B(\rho, c) + \frac{\lambda}{2}|\nabla\rho|^2 + \frac{\rho\varepsilon^2}{2}|\nabla c|^2. \quad (1)$$

The free energy Ψ_M extends the local free energy of a single-component compressible fluid Ψ_V[11] adding the mixing energy of NCG with the two phases of water (B/M_s) and square gradient terms that represent interfacial energies.[12] The interfacial energies lead to surface tensions at the liquid–vapor and liquid–NCG interfaces, whose values scale with λ and ε, respectively.[12] The function Ψ_V may be convex or non-convex, and this leads to equations of state like Peng–Robinson[13] or van der Waals[14] for pristine fluids. When Ψ_V is convex, solutions with uniform density are stable. When Ψ_V is

non-convex, the flow spontaneously separates into lower-density (the vapor phase) and larger-density (the liquid phase) regions. Vapor and liquid are separated by a diffuse interface, which regularizes the equations such that they remain well posed even in the spinodal region of the phase diagram.[15]

An important feature of the mixing dynamics of this problem is that NCG are much more miscible with the vapor phase of water than with its liquid phase. In our model, the function $B(\rho, c) = g(\rho)f_l(c) + [1 - g(\rho)]f_v(c)$ controls the NCG miscibility with the liquid and vapor phases of water. The equilibrium concentrations of NCG in the liquid and vapor water phases (namely, c_l^{eq} and c_v^{eq}, where $c_l^{eq} \ll c_v^{eq}$) are obtained from the functions f_l and f_v, which represent mixing energies of NCG with liquid water and water vapor, respectively.[16,17] The function $g(\rho) = (\rho_v - \rho)/(\rho_v - \rho_l)$ provides an interpolation between the liquid and the vapor phases of water.[12] The quantities ρ_v and ρ_l represent approximations to Maxwell states—equilibrium densities for the vapor and liquid phases at a given temperature, which can be obtained through variational calculus; for details, see the supplementary material. The balance laws for isothermal conditions represent the conservation of mass and linear momentum of the mixture, and conservation of mass of NCG, that is,

$$\dot{\rho} + \rho\nabla\cdot\boldsymbol{v} = 0, \quad \rho\dot{\boldsymbol{v}} = \nabla\cdot\boldsymbol{\sigma}, \quad \rho\dot{c} + \nabla\cdot\boldsymbol{j} = 0, \tag{2}$$

where $\boldsymbol{v}$ is the velocity field and a dot indicates material derivative. The Cauchy stress tensor $\boldsymbol{\sigma}$ and the NCG mass flux $\boldsymbol{j}$ follow from the application of the Coleman–Noll procedure with minimal assumptions, which ensures that the free energy in Eq. (1) decreases with time for any arbitrary process that satisfies the balance laws. The NCG mass flux and the Cauchy stress tensor take on the form[12]

$$\boldsymbol{j} = -\kappa\nabla\left[\frac{1}{\rho}\left(\frac{1}{M_s}\frac{\partial B}{\partial c} - \varepsilon^2\nabla\cdot(\rho\nabla c)\right)\right], \tag{3}$$

$$\boldsymbol{\sigma} = -p\boldsymbol{I} + \mu(\nabla\boldsymbol{v} + \nabla\boldsymbol{v}^T) + \eta\nabla\cdot\boldsymbol{v}\boldsymbol{I} + \boldsymbol{\zeta}_c + \boldsymbol{\zeta}_\rho. \tag{4}$$

Here, κ and M_s are the NCG diffusion constants. M_s is related to the rate of diffusion of NCG driven by the miscibility contrast of NCG between the liquid and vapor phases such that a smaller value of M_s implies a higher rate of buildup of NCG in vaporous regions. $\boldsymbol{I}$ is the identity tensor, μ and $\eta = -2\mu/3$ are the viscosity coefficients related by the Stokes' hypothesis; see Ref. 18 for a detailed analysis of the influence of bulk viscosity on the damping rate and the resonance frequencies of a bubble. The pressure is given by

$$p = \rho\psi_V' - \psi_V - \frac{1}{M_s}\left(B - \rho\frac{\partial B}{\partial\rho}\right), \tag{5}$$

the tensor $\boldsymbol{\zeta}_\rho = -\lambda\nabla\rho\otimes\nabla\rho + \lambda(\frac{1}{2}|\nabla\rho|^2 + \rho\nabla^2\rho)\boldsymbol{I}$ is the Korteweg stress, which accounts for the stresses developed at the liquid–vapor interface, and $\boldsymbol{\zeta}_c = -\rho\varepsilon^2\nabla c\otimes\nabla c$ represents the interfacial stress at the water–NCG interface.

To fully specify the model, we have to give expressions for Ψ_V and the functions f_l, f_v that define B. We take

$$\psi_V(\rho) = R\theta\rho\ln\left(\frac{\rho}{b-\rho}\right) - \frac{ab\rho}{2\sqrt{2}}\ln\left(\frac{\rho - b\left(1-\sqrt{2}\right)}{\rho - b\left(1+\sqrt{2}\right)}\right),$$

where θ is the temperature, R is the gas constant, and a, b are two additional parameters. Using Eq. (5) and the definition of Ψ_V, we obtain Peng–Robinson's equation of state[13] when NCG are not considered ($B = 0$); thus, the parameters a and b can be obtained from the critical properties of the fluid.[13] We define the functions f_l and f_v in B, leveraging Wilson's classical work;[16] thus,

$$f_{l,v}(c) = f_{\mathrm{id}}(c) - c\ln\left[c + \alpha_{l,v}(1-c)\right] - (1-c)\ln\left[1 - c + \beta_{l,v}c\right],$$

where $f_{\mathrm{id}}(c) = c\ln(c) + (1-c)\ln(1-c)$ represents the mixing energy of ideal gases and the remaining terms account for the non-ideal gas effects and the different miscibility of NCG in the liquid and vapor phases of water; $\alpha_{l,v}$ and $\beta_{l,v}$ are the dimensionless parameters of the model that determine the equilibrium concentrations of NCG in the liquid and vapor phases of water.

The model predicts phase transformations without pre-assumptions on the underlying mechanisms, and we are able to match the results of cavitation benchmarks in the absence of NCG, as shown in the supplementary material. More importantly, the model offers a path to understand the role of NCG dynamics in mass transfer. By introducing the vapor volume fraction $\alpha = (1-c)(\rho_l - \rho)/(\rho_l - \rho_v)$ and using conservation of mass of the mixture ($\dot{\rho} + \rho - \boldsymbol{v} = 0$) and conservation of NCG mass ($\rho\dot{c} + \nabla\cdot\boldsymbol{j} = 0$), we derive an equation for the time evolution of the vapor volume fraction,

$$\frac{\partial\alpha}{\partial t} + \nabla\cdot(\alpha\boldsymbol{v}) = \frac{\rho_l}{\rho_l - \rho_v}\left[(1-c)\nabla\cdot\boldsymbol{v} + \left(\frac{1}{\rho} - \frac{1}{\rho_l}\right)\nabla\cdot\boldsymbol{j}\right]. \tag{6}$$

Equation (6) provides a mechanistic understanding of the role of NCG on liquid–vapor mass transfer. It shows that the rate of change of the vapor volume fraction in the presence of NCG is obtained adding two contributions. We call the first one, $(1-c)\nabla\cdot\boldsymbol{v}$, hydrodynamic cavitation, and the second one, $(\rho^{-1} - \rho_l^{-1})\nabla\cdot\boldsymbol{j}$, mixing cavitation. Equation (6) also allows us to compare mass transfer in a mixture of a phase-transforming fluid and NCG with mass transfer in a single-component fluid ($c = \nabla\cdot\boldsymbol{j} = 0$). The presence of NCG alters mass transfer by two mechanisms: First, the factor $(1-c)$ reduces the mass transfer produced by hydrodynamic cavitation. Second, mixing cavitation can reduce or increase mass transfer depending on the local rate of change of NCG concentration.

To quantify and further understand the role of hydrodynamic and mixing cavitation, we run simulations on a one-dimensional tube of length 1 mm, initially filled with liquid water ($\rho = 1000\,\mathrm{kg/m^3}$) at temperature 292 K. We take both liquid–vapor and liquid–gas surface tension equal to 0.075 N/m, which gives us $\lambda = 1.6\times10^{-11}\ \mathrm{m^7\,kg^{-1}\,s^{-2}}$ and $\varepsilon = 1.38\times10^{-4}\ \mathrm{m^2/s}$. The parameter $\kappa = 2.3\times10^{-4}\ \mathrm{kg\,s/m^3}$ was chosen using experimental values for gas diffusivity for the rectified diffusion of gases,[19] and we take $M_s = 0.083\ \mathrm{s^2\,m/kg}$. The liquid is escaping from the tube on both sides with a velocity of 100 m/s. The simulations were performed using isogeometric analysis;[20] for more details, see the supplementary material. In this simulation, the rapid outflow of the fluid from both sides produces an expansion at the center, thereby causing conversion from liquid to vapor. This problem has been widely studied for single-component cavitation, and the literature results[8,21] quantitatively coincide with our model results when NCG is not considered ($c = 0$ in all equations); see the supplementary material. To understand the impact of NCG on mass transfer, we perform a simulation in which the fluid contains uniformly dissolved NCG with concentration equal to 3% of the saturation NCG concentration in the liquid phase of water, that is, $c(x, 0) = 0.03c_l^{eq}$.

Figure 1(a) shows the fluid density, NCG concentration, and velocity distributions in the tube. Because of conversion from liquid to vapor, the density inside the cavity becomes equal to the vapor density ρ_v and remains fairly constant in time. This lower-density region expands with time. There is diffusion of NCG from the liquid into the vaporous cavity, owing to the higher miscibility of NCG with the vapor phase of water. This rate of diffusion is primarily controlled by the diffusion parameter M_s, and a decrease in M_s would increase the rate of influx of NCG. The local rate of increase in NCG concentration inside the cavity remains fairly constant in time and increases as we approach the center of the tube. Figure 1(b) shows the hydrodynamic and mixing components of liquid–vapor mass transfer in the tube. Hydrodynamic cavitation plays a dominant role in this case, as the opening of the cavity is facilitated by a strongly divergent velocity field. The value of the hydrodynamic cavitation is zero outside the cavity and increases steeply at the cavity wall. The NCG accumulates at the center of the cavity, as seen in Fig. 1(a), and its presence reduces the value of hydrodynamic cavitation, owing to the factor $(1-c)$ in Eq. (6). The role of mixing cavitation is to oppose liquid–vapor conversion in this case, as evidenced by its negative value inside the cavity. This is because of the influx of NCG from the liquid into the vapor cavity. The extent of opposition to liquid–vapor conversion increases even more if the value of M_s is smaller. We can also see that the value of hydrodynamic cavitation diminishes as time evolves because $\nabla \cdot \boldsymbol{v}$ decreases as the cavity expands. The magnitude of mixing cavitation, however, is primarily governed by the local rate of increase in NCG concentration $\partial c/\partial t$, which remains almost constant throughout the simulation.

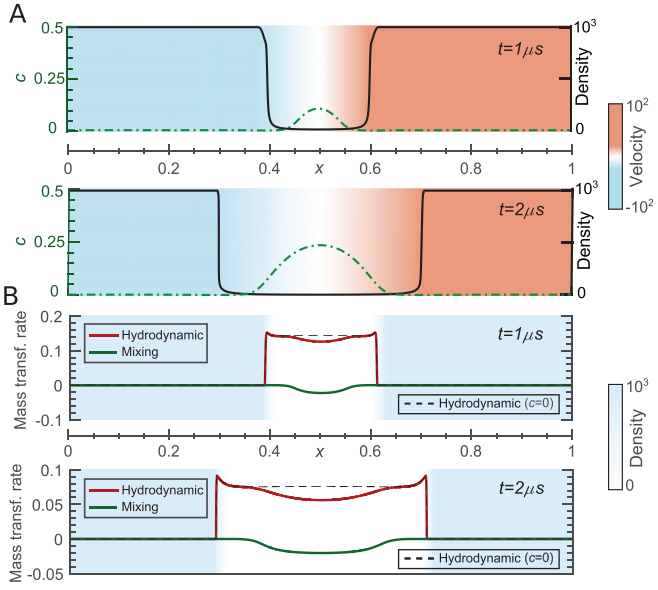

FIG. 1. (a) Fluid density (solid black line), NCG concentration (dashed green line), and fluid velocity (color scale) in the tube. (b) Hydrodynamic (red line) and mixing (green line) components of cavitation superimposed to the density field (color scale). The black dashed line represents hydrodynamic cavitation in the absence of NCG. We use the parameters $\mu = 1.15 \times 10^{-3}$ kg m^{-1} s^{-1}, $\lambda = 1.6 \times 10^{-11}$ m^7 kg^{-1} s^{-2}, $\varepsilon = 1.38 \times 10^{-4}$ m^2/s, $M_s = 0.083$ s^2 m/kg, $\kappa = 2.3 \times 10^{-4}$ kg s/m^3, $\alpha_l = \beta_g = 1$, $\alpha_g = \beta_l = 10^6$, $b = 1047.75$ kg/m^3, and $a = 544.011$ m^5 kg^{-1} s^{-2}. The mesh is composed of 2048 quadratic elements.

Our simulation in the 1D tube suggests that the presence of NCG only produces small changes in the cavitation rate. Also, the presence of NCG always reduces mass transfer from liquid to vapor in the 1D tube. We hypothesize, however, that mixing cavitation can increase the mass transfer rate and dominate hydrodynamic cavitation when the fluid has gas nuclei. We test this hypothesis by simulating vortex-induced cavitation in the presence of a small gas nucleus. We generate a vapor bubble using a Gaussian vortex with large circulation.[22–24] Under the assumption of single-component flow ($c = 0$), our model matched experimental results as shown in the supplementary material, but here we are interested in quantifying hydrodynamic and mixing cavitation in the presence of gas nuclei. We run simulations on a square box of side length 1 μm at temperature 292 K. We take both liquid–vapor and liquid–gas surface tension equal to 0.075 N/m, which gives us $\lambda = 1.6 \times 10^{-11}$ m^7 kg^{-1} s^{-2} and $\varepsilon = 1.55 \times 10^{-5}$ m^2/s. We take[19] $\kappa = 2.3 \times 10^{-4}$ s kg/m^3 and $M_s = 0.083$ s^2 m/kg. At the center of the box, there is a gas nucleus with a radius of 10 nm; which has a density of 2 kg/m^3, and NCG concentration equal to saturation concentration in the vapor phase, i.e., $c_v^{eq} = 0.9025$. The rest of the box is filled with liquid water ($\rho = 1000$ kg/m^3), with a uniform mass fraction of dissolved NCG ($c = c_l^{eq} = 0.0975$). The initial ($t = 0$) vortex[25] is given by the polar velocity field $\boldsymbol{v}_r = 0$, $\boldsymbol{v}_\varphi(r) = \frac{\Gamma_0}{2\pi r}(1 - e^{\gamma(r/r_c)^2})$, where (r, φ) are polar coordinates. The total circulation of the initial vortex is $\Gamma_0 = 4.71 \times 10^{-5}$ m^2/s, its core radius $r_c = 10$ nm and $\gamma = 1.255$. The strong rotation of the vortex creates a core of low pressure around the vortex centerline, which induces phase transformation from liquid to vapor. Figure 2 shows the time evolution of density and

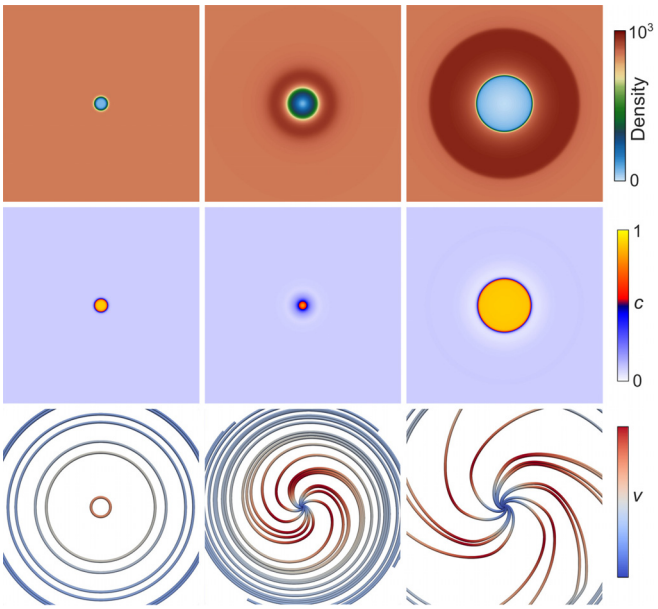

FIG. 2. Density (top row), NCG concentration (middle row), and velocity streamlines (bottom row) at $t/\tau_v = 0$ (left column), 0.1706 (central column), and 0.3412 (right column). Here, $\tau_v = 2\pi r_c / v_{max}$ is the vortex timescale,[22] where v_{max} is the maximum tangential velocity. We used the parameters $\mu = 1.15 \times 10^{-3}$ kg m^{-1} s^{-1}, $\lambda = 0.16 \times 10^{-12}$ m^7 kg^{-1} s^{-2}, $\varepsilon = 1.55 \times 10^{-5}$ m^2/s, $M_s = 0.083$ s^2 m/kg, $\kappa = 2.3 \times 10^{-4}$ s kg/m^3, $\alpha_l = \beta_g = 1$, $\alpha_g = \beta_l = 10^6$, $b = 1047.75$ kg/m^3, and $a = 544.011$ m^5 kg^{-1} s^{-2}. The mesh is composed of 4096 × 4096 quadratic elements.

concentration of NCG. The left column shows the initial conditions of the simulation. The central panel shows an initial decrease in density in the region around the gas nucleus. The nucleus is initially saturated with gas, which produces diffusion of NCG from the nucleus into a surrounding region with density lower than liquid density but higher than vapor density. There is, therefore, a decrease in the concentration of NCG at the center, as seen in the central panel. The rate of decrease in concentration of NCG decreases with a decrease in the diffusion constants κ and M_s. With the passage of time, we observe further lowering of the density in the region adjacent to the gas nucleus until the density becomes equal to vapor density. At this point, NCG starts to diffuse from the surrounding liquid into the expanding bubble. Also, we can observe an increase in density in the region around this expanding bubble. At equilibrium, an NCG-vapor bubble of constant radius is formed.

Figure 3 shows the magnitude of hydrodynamic and mixing cavitation at early times in the simulation. Figure 3(a) shows that at the earliest stages of the process, the rate of conversion from liquid to vapor inside the bubble is mostly governed by the mixing component of cavitation, which is more than two orders of magnitude larger than hydrodynamic cavitation. At this time, there is diffusion of NCG from the nucleus into the surrounding region of comparatively higher density. This leads to a positive value of the mixing cavitation term, which in this case facilitates cavitation as hypothesized. As time evolves, however, the magnitude of mixing cavitation inside the bubble keeps decreasing, and hydrodynamic cavitation plays a more prominent role; see Fig. 3(b). This is due to a decrease in the rate of NCG diffusion from the bubble to the surrounding liquid. Figure 3(c) shows the time evolution of the cumulative (spatial integral) contribution of hydrodynamic and mixing cavitation to the liquid-to-vapor (positive) mass transfer. The streamline plots in Fig. 2 also well illustrate the growth of hydrodynamic cavitation. Initially, the velocity field is divergence free. The divergent pattern in the streamlines that develops thereafter points to a non-solenoidal velocity field that induces phase change via hydrodynamic cavitation; see Eq. (6). The divergence of the velocity keeps growing with time, thereby increasing the contribution of hydrodynamic cavitation to the total rate of mass transfer. These flow patterns can be used to determine regions of the fluid where phase change is likely to occur.

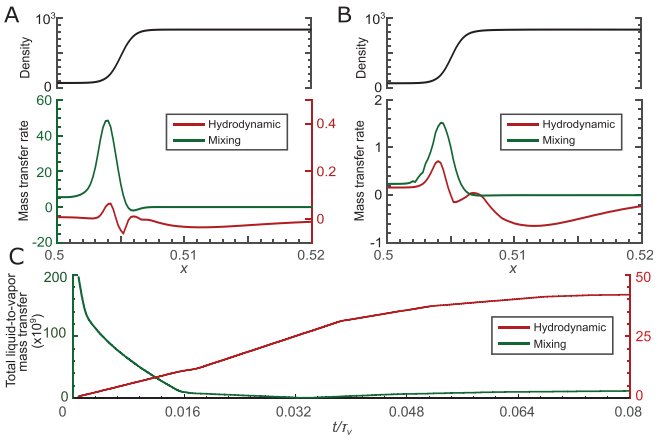

FIG. 3. Density (black), hydrodynamic (red), and mixing (green) mass transfer rates at $t/\tau_v = 8.5301 \times 10^{-4}$ (panel a) and 0.1706×10^{-1} (panel b), along $y = 0.5\ \mu$m. (c) Early time evolution of the magnitude of total mass transfer due to hydrodynamic (red) and mixing (green) cavitation from $t/\tau_v = 0$ to 0.08. The initial liquid-to-vapor phase change inside the bubble is dominated by mixing cavitation, but the hydrodynamic component prevails later in the process.

In conclusion, we have presented a unique combination of theory and simulations to provide mechanistic insight into how the presence of NCG modifies liquid–vapor mass transfer in cavitating fluids. Our results show that NCG always reduce hydrodynamic cavitation, but also give rise to what we call mixing cavitation, which may increase or reduce liquid–vapor mass transfer. Although our model and computations focus on idealized situations and more experimental evidence is warranted, this study may open a theoretical way to better understand cavitation in situations where NCG are likely to play an essential role. Prime examples of these situations are cavitation in micro-scale systems, sonoluminescence, and cavitation inception. Future efforts could focus on extending our deterministic model to thermally activated processes.

See the supplementary material for the details of equilibrium solutions of the model, derivation of surface tension at the liquid–vapor and liquid–gas interface, details of our numerical scheme, and validation cases for pure phase-transforming fluids without NCGs.

This work was funded in part by the U.S. Department of Defense (Award No. FA9550-20-1-0165) and by the National Science Foundation (Award No. CBET 1805817).

DATA AVAILABILITY

The data that support the findings of this study are available within the article and its supplementary material.

REFERENCES

[1]A. Prosperetti, "Vapor bubbles," Annu. Rev. Fluid Mech. **49**, 221–248 (2017).
[2]P. Prentice, A. Cuschieri, K. Dholakia, M. Prausnitz, and P. Campbell, "Membrane disruption by optically controlled microbubble cavitation," Nat. Phys. **1**, 107–110 (2005).
[3]H. Chen, W. Kreider, A. A. Brayman, M. R. Bailey, and T. J. Matula, "Blood vessel deformations on microsecond time scales by ultrasonic cavitation," Phys. Rev. Lett. **106**, 034301 (2011).
[4]M. S. Hutson and X. Ma, "Plasma and cavitation dynamics during pulsed laser microsurgery in vivo," Phys. Rev. Lett. **99**, 158104 (2007).
[5]B. H. Tan, H. An, and C.-D. Ohl, "How bulk nanobubbles might survive," Phys. Rev. Lett. **124**, 134503 (2020).
[6]A. Bussonnière, Q. Liu, and P. A. Tsai, "Cavitation nuclei regeneration in a water-particle suspension," Phys. Rev. Lett. **124**, 034501 (2020).
[7]M. Blander and J. L. Katz, "Bubble nucleation in liquids," AIChE J. **21**, 833–848 (1975).
[8]Q. Zheng, D. Durben, G. Wolf, and C. Angell, "Liquids at large negative pressures: Water at the homogeneous nucleation limit," Science **254**, 829–832 (1991).
[9]A. Amini, M. Reclari, T. Sano, M. Iino, M. Dreyer, and M. Farhat, "On the physical mechanism of tip vortex cavitation hysteresis," Exp. Fluids **60**, 118 (2019).
[10]F. Magaletti, L. Marino, and C. M. Casciola, "Shock wave formation in the collapse of a vapor nanobubble," Phys. Rev. Lett. **114**, 064501 (2015).
[11]L. D. Landau and E. M. Lifshitz, *Course of Theoretical Physics* (Elsevier, 2013).
[12]S. Mukherjee and H. Gomez, "Flow and mixing dynamics of phase-transforming multicomponent fluids," Appl. Phys. Lett. **115**, 104101 (2019).
[13]D.-Y. Peng and D. B. Robinson, "A new two-constant equation of state," Ind. Eng. Chem. Fundam. **15**, 59–64 (1976).

[14]J. D. van der Waals, "The thermodynamic theory of capillarity under the hypothesis of a continuous variation of density," J. Stat. Phys. **20**, 200–244 (1979).
[15]J. Liu, C. M. Landis, H. Gomez, and T. J. Hughes, "Liquid–vapor phase transition: Thermomechanical theory, entropy stable numerical formulation, and boiling simulations," Comput. Methods Appl. Mech. Eng. **297**, 476–553 (2015).
[16]G. M. Wilson, "Vapor-liquid equilibrium. XI. A new expression for the excess free energy of mixing," J. Am. Chem. Soc. **86**, 127–130 (1964).
[17]X. Fu, L. Cueto-Felgueroso, and R. Juanes, "Viscous fingering with partially miscible fluids," Phys. Rev. Fluids **2**, 104001 (2017).
[18]C. Scognamiglio, F. Magaletti, Y. Izmaylov, M. Gallo, C. M. Casciola, and X. Noblin, "The detailed acoustic signature of a micro-confined cavitation bubble," Soft Matter **14**, 7987–7995 (2018).
[19]L. A. Crum, "Measurements of the growth of air bubbles by rectified diffusion," J. Acoust. Soc. Am. **68**, 203–211 (1980).
[20]T. J. Hughes, J. A. Cottrell, and Y. Bazilevs, "Isogeometric analysis: CAD, finite elements, NURBS, exact geometry and mesh refinement," Comput. Methods Appl. Mech. Eng. **194**, 4135–4195 (2005).
[21]R. Saurel and O. Lemetayer, "A multiphase model for compressible flows with interfaces, shocks, detonation waves and cavitation," J. Fluid Mech. **431**, 239–271 (2001).
[22]J. Choi, C.-T. Hsiao, G. Chahine, and S. Ceccio, "Growth, oscillation and collapse of vortex cavitation bubbles," J. Fluid Mech. **624**, 255–279 (2009).
[23]J. Choi and S. L. Ceccio, "Dynamics and noise emission of vortex cavitation bubbles," J. Fluid Mech. **575**, 1–26 (2007).
[24]R. E. Arndt and A. P. Keller, "Water quality effects on cavitation inception in a trailing vortex," J. Fluids Eng. **114**, 430–438 (1992).
[25]G. Oweis, I. Van der Hout, C. Iyer, G. Tryggvason, and S. Ceccio, "Capture and inception of bubbles near line vortices," Phys. Fluids **17**, 022105 (2005).